Midinfrared thermal emission properties of finite arrays of gold dipole nanoantennas

M. Centini, A. Benedetti, M. C. Larciprete, A. Belardini, R. Li Voti, M. Bertolotti, and C. Sibilia
Dipartimento di Scienze di Base ed Applicate per l'Ingegneria, Sapienza Università di Roma, Via A. Scarpa 16, 00161 Roma, Italy
(Received 17 October 2014; revised manuscript received 2 October 2015; published 9 November 2015)

We studied the far-field thermal emission properties of finite arrays of resonant gold dipole nanoantennas at equilibrium temperature. We numerically investigated the transition from the super-Planckian emission of the single resonant antenna to the sub-Planckian emission inherent to infinite periodic arrays. Increasing the number of unit cells of the array, the overall size of the system increases, and the relative emissivity quickly converges to values lower than the unity. Nevertheless, if the separation between nanoantennas in the array is small compared to the wavelength, the near-field interaction makes the emission of each unit cell multipolar. This opens the doors for additional tailoring of the emitted power and directionality of thermal radiation.

DOI: 10.1103/PhysRevB.92.205411 PACS number(s): 44.40.+a, 65.80.−g, 78.67.−n, 42.72.Ai

I. INTRODUCTION

The possibility to control the infrared (IR) absorption and thermal emission on subwavelength scales has attracted large interest in the recent years thanks to the opportunities granted by nanostructured metamaterials (composed of plasmonic and/or semiconductor constituents) [1]. The development of nanofabrication techniques motivates researchers to pursue further studies of both convective/conductive and radiative heat transport on nano- and microscales [2–4]. Thermal properties of nanostructured materials (including thermal emission and IR absorption) have been deeply investigated with the aim of enhancing and tailoring the properties of thermal radiation and radiative heat transfer. For example, high frequency selective and directional thermal emitters/absorbers have been proposed for a large variety of applications ranging from sensing and security [5,6] to cooling and energy harvesting [7–10].

The radiative heat exchange properties between nanostructures [11,12] and between macroscopic systems separated by nanogaps [13] have been extensively studied for a long time [14,15]. Recently, it has been experimentally shown that the thermal radiation exchanged between two hot bodies out of thermal equilibrium, separated by small distances compared with the corresponding thermal wavelengths, can exceed the Stefan-Boltzmann law by three orders of magnitude [16]. In these cases, the corresponding thermal emission is called super-Planckian to emphasize that it can go beyond the classical black-body theory [17]. The possibility of obtaining super-Planckian far-field thermal emission in resonant nanoantennas (NAs) has been investigated as well. The properties of the spectrum, coherence, polarization, and angular distribution of the far-field thermal radiation emitted by NAs of different shapes and materials have been studied [18–20]. In particular, the enhanced dipolar antennalike thermal emission from dielectric [21] and metallic [22] NAs has been experimentally observed. Also, scattering and absorption cross sections of individual gold NAs have been recently measured using a quantitative phase-sensitive modulation technique [23]. Although the emissivity of a single dipole NA, at its resonance frequency, can exceed the black-body limit by 1–2 orders of magnitude, this super-Planckian emission has a typical dipole radiative pattern. On the other hand, infinite arrays of resonant NAs and gratings can be designed in order to achieve large spatial and temporal coherence of the emitted radiation (i.e., quasimonochromatic and highly directional emission) [24,25]. Nevertheless, both theoretical calculations and experiments confirmed that the normalized emissivity of infinite, periodic arrays of isothermal NAs never exceeds unity. However, the evolution of thermal radiation properties along the transition from a single NA to an infinite periodic array of NAs reveals interesting features that have not been previously studied in details.

In this paper, we analyze different configurations of finite resonant NA arrays in the 1–5 μm wavelength range. For our paper, we adapted and implemented a simple model based on the Green dyadic and on the numerical solution of the resulting volume integral equation (VIE) to calculate the far-field thermal emission pattern of either one or a small ensemble of NAs (oligomers). Green methods have been extensively used for analytical calculations of thermal radiation from multilayers, spheres, cylinders, and pointlike dipoles [1,12,14,15]. However, with complex geometries, higher order multipoles can significantly contribute to the radiative spectrum and pattern [23], thus numerical brute-force approaches are necessary in order to obtain reliable results [26,27]. A clear, brief, and updated overview of the most commonly used numerical techniques is also presented in Ref. [4].

After a quick validation of our method (comparing the numerical results with the analytically calculated relative emissivity of a gold isothermal sphere) and a brief report on the thermal emission properties of a single NA, we study the behavior of finite arrays of NAs as a function of the number of elements in the array and of the separation distance between NAs. We distinguish two regimes: when the distance between elements is (a) comparable to their resonant wavelength, of the order of 1 μm, or (b) shorter than the wavelength, i.e., a few dozens of nm. In the first case, the elements are weakly coupled by evanescent waves and mainly behave as individual sources. Thus, the emission spectrum is similar to the one of the single emitter, and the relative emissivity, normalized with respect to the total surface, quickly converges to the limit for infinite arrays. On the other hand, when the distance between elements is of the order of 10 to 100 nm, multipolar magnetic and electric resonances arise from evanescent wave coupling between adjacent unit cells [28,29]. Indeed, the system behaves as a composite antenna with new resonant peaks with respect to the single element features due to mode hybridization. We will show that this peculiarity offers us additional possibilities

to tailor the thermal radiation. We finally provide an example to show that emission from such dense arrays of NAs can be optimized in a tradeoff between high directionality and high emitted power.

II. SINGLE RESONANT NA

We begin our paper with the characterization of the thermal emission properties of a single gold NA. For all of the calculations, we used the refractive indices from Palik [30]. As a first step, we briefly introduce the adopted numerical method; more details can be found in the Appendix. For the purpose of calculating ensemble-averaged mean radiated power in the far field, we need to evaluate the cross spectral density, defined as

$$\bar{\bar{W}}_\omega(\vec{r}_1,\vec{r}_2)\delta(\omega-\omega') = \langle \vec{E}_\omega(\vec{r}_1)\vec{E}^\dagger_{\omega'}(\vec{r}_2)\rangle, \tag{1}$$

where † indicates the Hermitian operator and the brackets represent a statistical ensemble average. In the far-field regime, the diagonal elements of the cross spectral density $\bar{\bar{W}}_\omega(\vec{r}_1,\vec{r}_1)$ are proportional to the mean radiated intensity spectral density. In the Appendix we show that the cross spectral density can be numerically evaluated on a discretized mesh as a product between an auxiliary deterministic matrix $\bar{\bar{K}}$, taking into account for the scattering problem, and the cross correlation function of the fluctuating sources given by the fluctuation dissipation theorem [15]:

$$\overline{\overline{W}} = \langle \bar{X}\bar{X}^\dagger\rangle = \bar{\bar{K}}^{-1}\langle \bar{B}\bar{B}^\dagger\rangle \bar{\bar{K}}^{-1^\dagger}, \tag{2}$$

where

$$\bar{X} = \left(E_1^x, E_2^x, \ldots, E_{N_s}^x, E_1^y, E_2^y, \ldots, E_{N_s}^y, E_1^z, E_2^z, \ldots, E_{N_s}^z\right) \tag{3}$$

is the total field evaluated on the discretized mesh, identified by a set of points $i = 1,2,\ldots,N_s$ being N_s the number of the mesh points. $\bar{\bar{K}}$ is a $3N_s \times 3N_s$ scattering matrix, and the matrix operator $\langle \bar{B}\bar{B}^\dagger\rangle$ contains all the information on the thermal sources. In the Appendix, we derive the expression for $\bar{\bar{K}}$, and we show that $\langle \bar{B}\bar{B}^\dagger\rangle$ is the discretized counterpart of the following quantity:

$$\langle \vec{E}_{inc,\omega}(\vec{r}_1)\vec{E}^\dagger_{inc,\omega'}(\vec{r}_2)\rangle = \mu_o^2\,\omega^2 \int \overline{\overline{G}}_\omega(\vec{r}_1,\vec{r}')\,\overline{\overline{G}}^\dagger_{\omega'}(\vec{r}_2,\vec{r}'')\left\langle \vec{J}^0_\omega(\vec{r}')\,\vec{J}^{0\dagger}_{\omega'}(\vec{r}'')\right\rangle d\vec{r}'d\vec{r}'', \tag{4}$$

where μ_0 is the vacuum magnetic permeability and $\bar{\bar{G}}_\omega$ is the Green dyadic for the vacuum. Also, from the fluctuation dissipation theorem, we show that the correlation function of fluctuating currents for an anisotropic, local, and nonmagnetic medium with time-reversal symmetry at local thermal equilibrium can be expressed as [15]

$$\left\langle \vec{J}^0_\omega(\vec{r}')\,\vec{J}^{0\dagger}_{\omega'}(\vec{r}'')\right\rangle = \frac{\omega}{\pi}\varepsilon_0 \mathrm{Im}(\varepsilon_{r,\omega})\Theta_\omega(T)\delta(\vec{r}'-\vec{r}'')\delta(\omega-\omega')\overline{\overline{I}}, \tag{5}$$

Being:

$$\Theta_\omega(T) = \frac{\hbar\omega}{\exp(\hbar\omega/k_BT)-1}, \tag{6}$$

where $\hbar$ is the reduced Planck's constant, k_B is the Boltzmann constant, T is the temperature, ε_0 is the vacuum permittivity, and $\mathrm{Im}(\varepsilon_r)$ is the imaginary part of the material relative permittivity. The far-field emitted power is then evaluated by considering a sphere with a radius (R_{sp}) much larger than both the wavelengths and the size of the emitting system under consideration. In these conditions, the evaluation of the cross spectral density on the sphere gives the far-field behavior of the system. The average power spectral density emitted by the source can be obtained by calculating

$$P_\omega = \frac{c\varepsilon_0}{2}\sum_{j=N_s+1}^{N_\Sigma} diag(\langle \bar{X}\bar{X}\rangle)_j \Delta\Sigma_j, \tag{7}$$

where Σ is the surface of the sphere, discretized by $j = N_s+1,2,\ldots,N_\Sigma$ points, related to surface patches $\Delta\Sigma_j$; $diag(\langle \bar{X}\bar{X}\rangle)_j$ is the jth diagonal element of the discretized cross spectral density that corresponds to points belonging to the surface of the sphere. The relative emissivity can be defined by normalizing the calculated power spectral density as a function of the wavelength ($P_\lambda = P_\omega \frac{2\pi c}{\lambda^2}$), with the one corresponding to a black body having the same overall surface (σ) of the considered sources:

$$P^{b.b.}_\lambda = \frac{2\pi hc^2\sigma}{\left(e^{\frac{hc}{\lambda KT}}-1\right)\lambda^5}. \tag{8}$$

For complex systems composed by different objects, σ is the smallest surface containing all the system. Finally the relative emissivity is given by

$$e_{r,\lambda} = \frac{P_\lambda}{P^{b.b.}_\lambda}. \tag{9}$$

As a benchmark test for the accuracy and reliability of our method, we considered the simple case of a single isothermal Au sphere of diameter equal to 20 nm. In this case, it is possible to calculate an analytical solution for the relative emissivity, as defined in Eq. (9), by applying the Mie scattering theory. In particular, the relative emissivity of an isothermal sphere is given by its absorption efficiency [31]. In Fig. 1, we plot the comparison between the results of our numerical calculations and the analytically evaluated absorption efficiency from Mie scattering theory. We notice that the results obtained with the two different methods are in reasonable agreement. Small discrepancies could be related to the spurious roughness of the surface of the sphere introduced by the mesh discretization.

Finally, we apply the numerical method to a linear dipole NA (sketched in the inset of Fig. 2) with a length of 505 nm and rectangular section of (33 nm × 83 nm), at a temperature T, embedded in vacuum. The length of the NA has been chosen according to the resonance maps reported in Ref. [32] in order to have a resonance wavelength of approximately 2 μm. In Fig. 2, we plot the calculated relative emissivity as a function of the wavelength. As expected, we note that the maximum emissivity is achieved at the resonance wavelength $\lambda = 2.1\,\mu$m. We also note that the maximum value is greater than unity, confirming the super-Planckian behavior. The role of the NA, leading to enhanced far-field emissivity at resonance, is both to provide an increased value of the local density of states (enhancing the emission) and to efficiently couple the evanescent components of the emitted field to propagating modes that form the far-field radiating pattern.

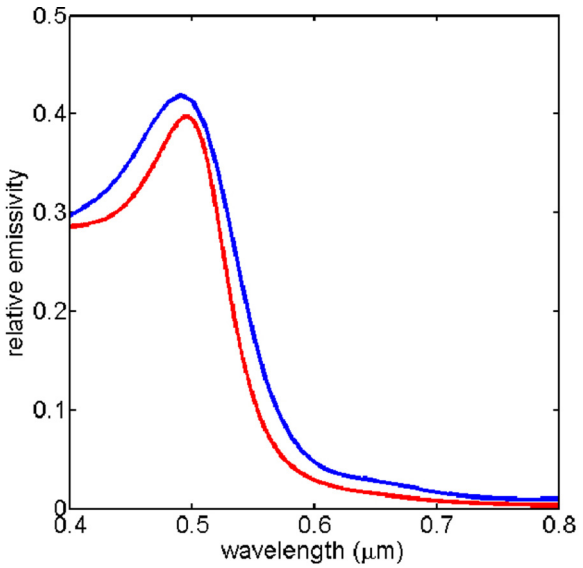

FIG. 1. (Color online) Relative emissivity calculated for a 10 nm radius gold sphere using Mie scattering theory (red line) and our numerical method based on the solution of the volume integral equation (blue line).

We also show in Fig. 3 the emission pattern in $W/(\text{sr m})$ at $\lambda = 2.1\,\mu$m when the antenna, embedded in vacuum, is at an equilibrium temperature of 900 K. We note the typical electric dipole (ED) emission pattern. Also, for all the directions in the xy plane, the emission is nearly 100% polarized with the electric field oscillating along the z axis.

III. FINITE PERIODIC ARRAYS

We compare the far-field relative emissivity of arrays of resonant NAs composed of two, three, and four elements with

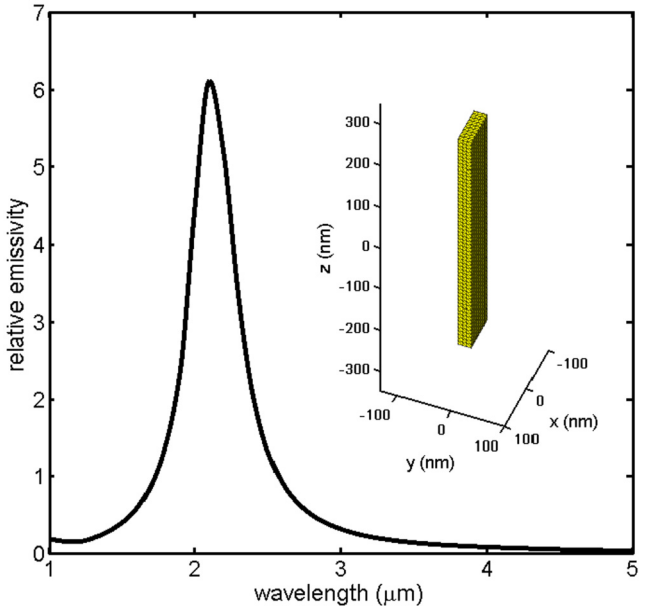

FIG. 2. (Color online) Relative emissivity as a function of wavelength calculated for the Au dipole NA sketched in the inset.

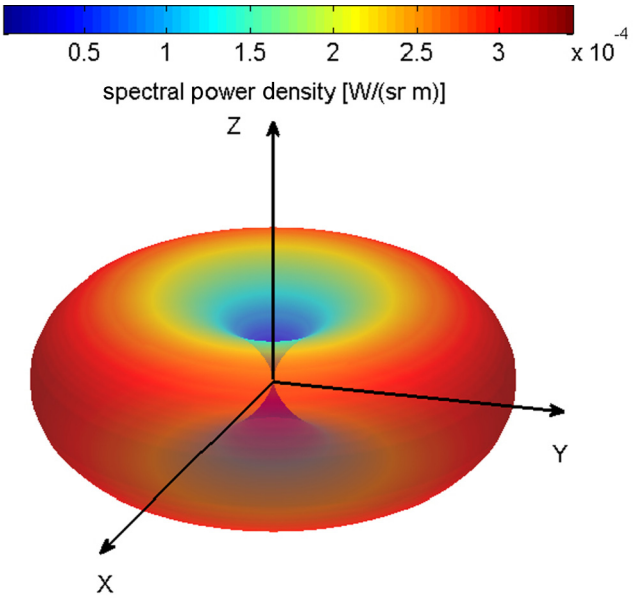

FIG. 3. (Color online) Thermal emission pattern of the spectral power density corresponding to the maximum emission wavelength ($\lambda = 2.1\,\mu$m) for the Au NA, depicted in Fig. 2 at an equilibrium temperature $T = 900$ K, embedded in vacuum.

respect to the relative emissivity of the previously analyzed single element. The arrays are realized by considering periodic repetition of aligned NAs along the y direction. The NA main axis is always oriented along the z direction. An example of the scheme of the array is depicted in Fig. 4(a). In order to calculate the relative emissivity, we normalize the radiated power spectral density with respect to the power spectrum corresponding to an ideal black body at the same temperature of the system, with an effective surface equal to the surface of the minimum box containing the entire system, as sketched in Fig. 4(b). According to this definition, if A, B, and C are the dimensions of the single NA and D is the distance between elements, the N-element array will have an effective surface

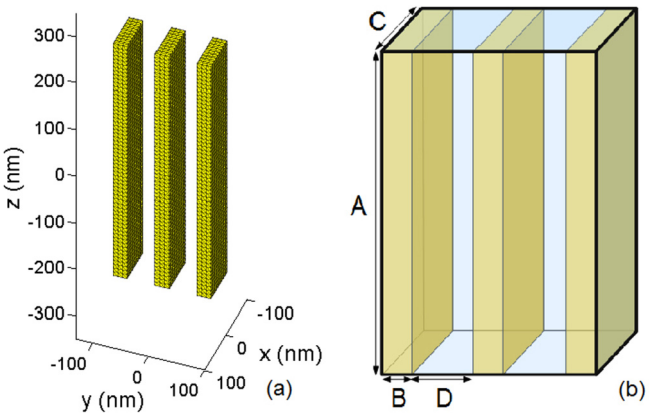

FIG. 4. (Color online) (a) Sketch of the array composed by three resonant NAs aligned along the y direction, with the main axis parallel to the z direction. (b) Definition of the effective surface of the box containing the antenna, used to calculate the normalized emissivity.

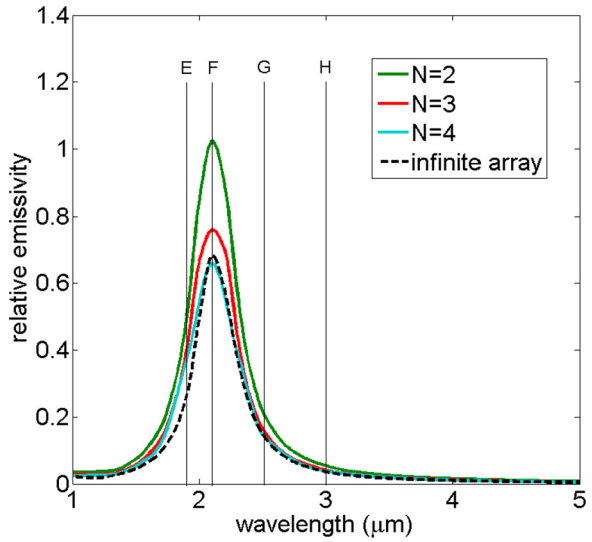

FIG. 5. (Color online) Relative emissivity as a function of wavelength calculated for arrays composed by two, three, and four resonant NAs separated by a distance of 900 nm. The dashed line represents the emissivity calculated for an infinite array in the approximation of independent sources. Markers E, F, G, and H refer to the wavelengths (1.9 μm, 2.1 μm, 2.5 μm, and 3.0 μm) corresponding to the radiative profiles that have been plotted in markers E, F, G, and H in Fig. 7, respectively.

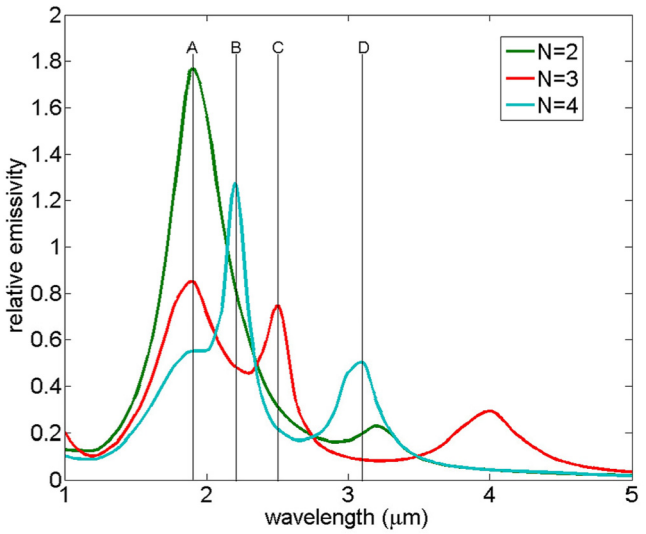

FIG. 6. (Color online) Relative emissivity as a function of wavelength calculated for arrays composed by two, three, and four resonant NAs separated by a distance of 75 nm. Markers A, B, C, and D refer to the wavelengths (1.9 μm, 2.2 μm, 2.5 μm, and 3.1 μm) corresponding to the radiative profiles that have been plotted in markers A, B, C, and D in Fig. 7, respectively.

equal to

$$S_N = NS_1 + 2(N-1)(A\cdot B + D\cdot C - A\cdot C), \qquad (10)$$

where S_1 is the surface of the single NA. The relative emissivity can be written as

$$e_{r,N} = \frac{P_N}{e_{b.b.}S_N}, \qquad (11)$$

where $e_{b.b.}$ is the black-body emissivity and P_N is the power emitted by the N-element array. In Fig. 5, we show the relative emissivity calculated for arrays composed by periodic repetition of the previously investigated NA. The separation between elements is 900 nm; we report numerical results for $N = 2,3,4$ elements. We note that the typical spectrum of the relative emissivity does not qualitatively change with respect to the emissivity of a single NA (see Fig. 2). However, the maximum value rapidly decreases, and the super-Planckian behavior disappears for $N \geq 3$. Indeed the NAs are distributed with a low spatial density (low filling factor), thus the increasing effective surface of the system (S_N) drastically reduces the relative emissivity, according to Eq. (10). Moreover, there is a weak evanescent wave coupling between adjacent NAs, and the overall system behaves, in good approximation, as a set of independent, partially coherent sources. In this regime, it is easily possible to establish a limit for infinite structures. Considering independent sources, the average power radiated by the N-element array can be written as $P_N = NP_1$, where P_1 is the power radiated by a single NA. By substituting Eq. (10) into Eq. (11) and considering $e_{r,1} = \frac{P_1}{e_{b.b.}S_1}$, the relative emissivity of the single NA, it can be easily shown that the relative emissivity for an infinite array of independent sources can be expressed as follows:

$$e_{r,\infty} = \lim_{N\to\infty}\left(\frac{NP_1}{e_{b.b.}S_N}\right) = e_{r,1}\frac{S_1}{2(A\cdot B + B\cdot C + A\cdot D + D\cdot C)}. \qquad (12)$$

The limit value for the emissivity calculated by using Eq. (12) is depicted in Fig. 5 with a dashed line. As expected, the results for finite arrays rapidly converge to the infinite array behavior.

A different scenario is presented when shorter separation distances between elements are considered. Indeed, the strong evanescent wave coupling between adjacent unit cells is responsible for the appearance of new resonances in analogy of hybrid bonding and antibonding modes in a molecule, for example. The system behaves as a composite antenna, and its properties are sensibly different with respect to those of the single NA. In Fig. 6, we report the results of our calculations performed for finite arrays composed of $N = 2,3,$ and 4 elements spaced by a distance of 75 nm from each other. We notice that because of the appearance of new resonances, the relative emissivity peaks do not necessarily decrease by increasing the number of elements. For example, in the considered wavelength spectrum, the relative emissivity of the three-element array is always lower than one, while the four-element array shows a super-Planckian sharp peak at a wavelength of 2.2 μm corresponding to a multipolar resonance of the system. However, we point out that this behavior is not in contradiction with our previous discussion, since the overall size of the four-element array is subwavelength (505 nm $\times$ 357 nm $\times$ 83 nm).

Recently it has been shown that the contributions of magnetic and electric resonances can boost directivity as well

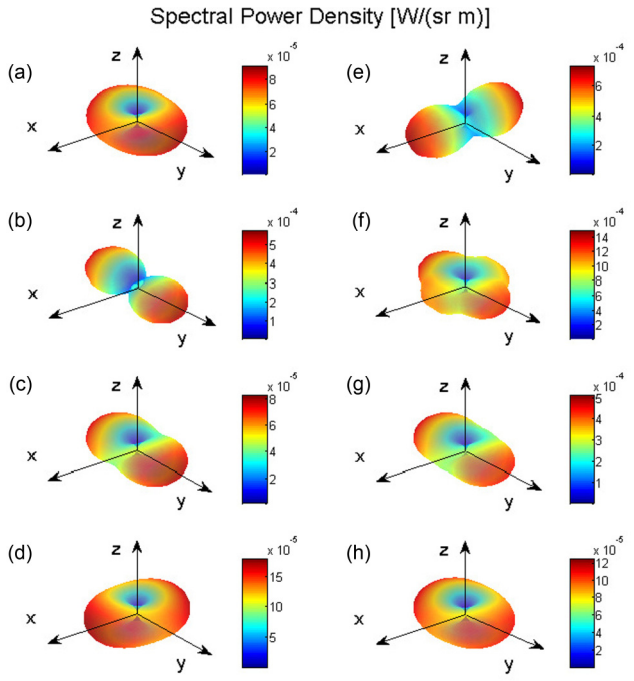

FIG. 7. (Color online) Calculated radiative patterns for the four-element NA arrays at an equilibrium temperature of 900 K corresponding to the wavelengths marked with A, B, C, and D in Fig. 6 for the arrays with separation distance of 75 nm and E, F, G, and H in Fig. 5 for the 900 nm spaced arrays.

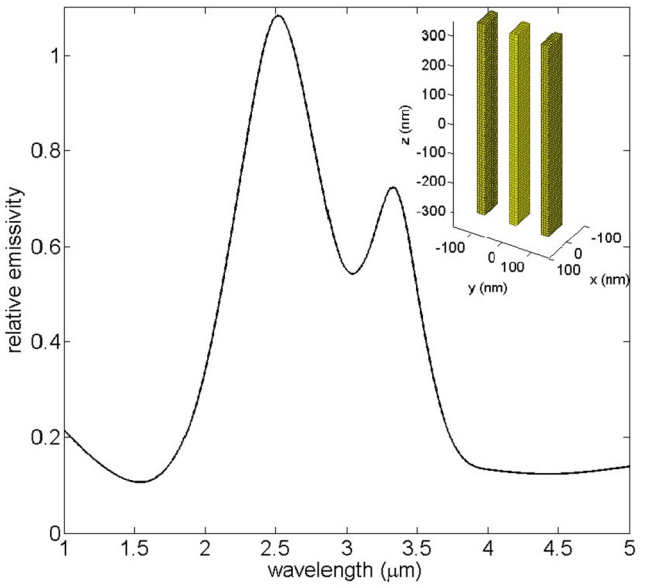

FIG. 8. (Color online) Relative emissivity as a function of wavelength calculated for the three coupled Au dipole NAs sketched in the inset.

as spatial asymmetry of the emission pattern of a dipole single emitter placed in the proximity of composite NAs [33]. In our case, the NA array is not fed by a deterministic point source; all the system behaves as an extended source. However, interesting features emerge by analyzing the corresponding thermal radiation patterns. In Fig. 7, we plot the radiative patterns calculated for the previously studied four-element arrays with separation distances of 900 nm and 75 nm at several wavelengths (marked with points A, B, C, and D and E, F, G, and H in Figs. 6 and 5, respectively). The calculation has been performed considering all the systems at the equilibrium temperature of 900 K. We note a strong dependence of the radiative patterns as a function of the wavelength. For the case of 900 nm, separation distance between NAs (see markers E, F, G, and H in Fig. 7) interference effects between the signals emitted by each NA are responsible for far-field radiative pattern changes. Indeed, individual NAs are partially coherent emitters since they have a resonant emission line at 2.1 μm with a bandwidth of approximately 400 nm. Thus, the radiation pattern is the result of a spatial redistribution of the energy, while the total spectral power density follows the resonant behavior of the single NA, as shown in Fig. 5.

A different mechanism is at the base of the shape of the radiative pattern for the four-element array with 75 nm separation distance (see markers A, B, C, and D in Fig. 7). The emission is dominated by multipolar modes, and their appearance is directly observable from the multiple peaks of the emissivity spectrum (Fig. 6). In particular, we note that the emission at 1.9 μm (Fig. 7, marker A) is mostly dominated by the ED contribution, while at 2.2 μm (Fig. 7, marker B) excitation of both magnetic dipoles (MDs) and EDs is responsible for a highly directional emission. From Fig. 6, we also note that the emission peak has a bandwidth of 200 nm, which is narrower than the bandwidth of the single NA resonance. According to Ref. [18], as the system size increases, the bandwidth of super-Planckian emission becomes narrower. Evanescent waves coupling between elements of the array makes it possible to tailor both the radiative spectrum and pattern by changing the parameters of the NA and their relative distances.

As an example, we studied the case of three gold dipole antennas, 655 nm long, with a (83 nm $\times$ 33 nm) rectangular section, placed at a distance of 85 nm from each other along the y direction, as sketched in the inset of Fig. 8. In the same figure, we depict the calculated relative emissivity as a function of wavelength. We note two different peaks: one centered at $\lambda_1 = 2.52\,\mu$m and the other at $\lambda_2 = 3.35\,\mu$m. Finally we plot in Fig. 9 the emission patterns in W/(sr m) at both λ_1 and λ_2 when the system, embedded in vacuum, is at an equilibrium temperature of 900 K. We note [Fig. 9(a)] that the emission pattern at λ_1 displays the typical ED pattern. On the other hand, the emission at λ_2 [Fig. 9(b)] is highly directional, mainly along the y axis. The radiative patterns are plotted on the same scale in order to highlight the strong directionality of the thermal emission at λ_2. The spectral linewidth of the emission at 3.35 μm is approximately 400 nm, and the angular divergence of each lobe is approximately 0.6 sr. The total size of the array is 655 nm $\times$ 83 nm $\times$ 269 nm.

In order to deeply understand the nature of this highly selective resonance, we plot the modulus of the z component of the electric field [Fig. 10(a)] and the modulus of the x component of the magnetic field [Fig. 10(b)] at $\lambda_2 = 3.35\,\mu$m when a plane incident z-polarized wave impinges along the y axis. We note the response of the antenna is mainly driven by two contributions: MD and ED. The magnetic resonance

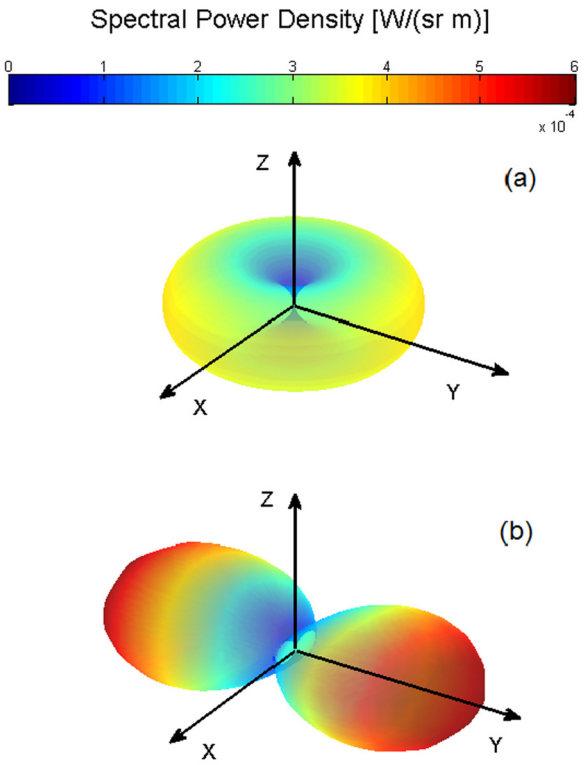

FIG. 9. (Color online) Thermal emission pattern of the spectral power density corresponding to (a) the ED resonance ($\lambda_1 = 2.52\,\mu$m) and (b) the MD resonance ($\lambda_1 = 3.35\,\mu$m) for the three coupled Au NAs depicted in the inset of Fig. 8 at an equilibrium temperature $T = 900$ K, embedded in vacuum.

is originated by current loops along the wires, closed by displacement currents in the spaces between wires. The current loops mainly lay in the yz plane, producing a magnetic field oscillating along the x axis. However, the response is also strongly driven along the z axis for what concerns the electric field. As a consequence of the transversality of plane electromagnetic (EM) waves, the coupling between propagating modes and the NA array, in the far-field regime, is maximized with an EM plane wave propagating along the y direction.

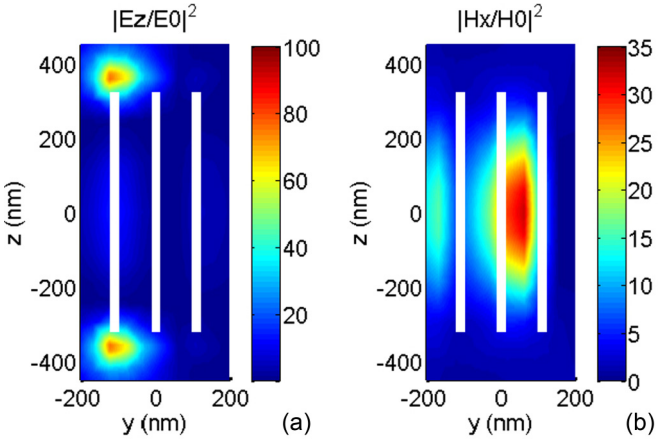

FIG. 10. (Color online) Normalized modulus of (a) the z component of the electric field, (b) the x component of the H field, with respect to the input field amplitudes. An impinging plane wave propagating along the y direction, z polarized at $\lambda_2 = 3.35\,\mu$m is considered. The fields are collected on a plane perpendicular to the x axis at a distance of 20 nm from the antenna.

IV. CONCLUSIONS

We numerically studied the thermal radiation from finite arrays of resonant NAs. The transition from the super-Planckian emission of the single NA at its resonance frequency to the sub-Planckian emission of infinite arrays was investigated. We put into evidence the role of evanescent wave coupling between elements. If the separation between NAs is small compared to the wavelength, new resonances appear due to mode hybridization, and the finite array behaves as a multipolar antenna. Increasing the number of unit cells, the emissivity converges to sub-Planckian values. Nevertheless, we have shown that considering a limited number of elements, contributions from ED and MD resonances can be tailored to optimize performances in a trade-off between high directionality and super-Planckian emission. As a further development, optimization could be performed by extending the study to nonisothermal systems and hybrid structures composed of both metallic and dielectric components.

ACKNOWLEDGMENT

M.C. kindly acknowledges Kristján Leósson and Grigore Leahu for inspiring discussions on the thermal emission properties of nanostructured surfaces.

APPENDIX

The numerical investigation was performed using a method based on the fluctuational electrodynamics approach and on the discretization of the resulting VIE. No approximation is adopted in the near field in order to take into account the evanescent waves coupling between objects and the excitation of higher order modes of the ensemble. Here we show how it is possible to express the radiated power by properly combining a deterministic scattering matrix with the fluctuation dissipation theorem expressed by the Callen-Welton equation. For a typical scattering problem, the electric field at frequency ω can be calculated by solving the following equation [34]:

$$\left(\overrightarrow{\nabla} \wedge \overrightarrow{\nabla} \wedge -\frac{\omega^2}{c^2}\bar{\bar{I}}\right)\vec{E}_\omega(\vec{r}) = i\omega\mu_0\vec{J}_\omega(\vec{r}), \qquad \text{(A1)}$$

where c is the speed of light in vacuum, μ_0 is the magnetic permeability, and $\bar{\bar{I}}$ is the identity operator. The generalized current density $\vec{J}_\omega(\vec{r})$ takes into account for both the geometry (the material properties) and additional impressed sources of the radiation field:

$$\vec{J}_\omega(\vec{r}) = -i\omega\varepsilon_0\chi_\omega(\vec{r})\vec{E}_\omega(\vec{r}) + \vec{J}^0_\omega(\vec{r}), \qquad \text{(A2)}$$

where ε_0 is the vacuum permittivity and $\chi_\omega(\vec{r})$ is the electric susceptibility of the scatterers. $\vec{J}^0_\omega(\vec{r})$ holds for other impressed current densities acting as sources of the EM field. The formal

solution of Eq. (A1) is given by

$$\vec{E}_\omega(\vec{r}) = \vec{E}_{inc,\omega}(\vec{r}) + \int_V k_0^2 \chi_\omega(\vec{r}')\bar{\bar{G}}_\omega(\vec{r},\vec{r}')\cdot\vec{E}_\omega(\vec{r}')d\vec{r}', \quad \text{(A3)}$$

where V is the volume of the scatterers, k_0 is the wavenumber (ω/c), and $\bar{\bar{G}}_\omega$ is the Green dyadic for the vacuum:

$$\bar{\bar{G}}_\omega(\vec{r},\vec{r}') = \frac{1}{4\pi}\left[\bar{\bar{I}} + \frac{1}{k_0^2}\vec{\nabla}\vec{\nabla}\right]\frac{e^{ik_0|\vec{r}-\vec{r}'|}}{|\vec{r}-\vec{r}'|} = \bar{\bar{G}}_\omega(\vec{R})$$
$$= \left(\bar{\bar{I}} + \frac{ik_0R-1}{k_0^2R^2}\bar{\bar{I}} + \frac{3-3ik_0R-k_0^2R^2}{k_0^2R^4}\vec{R}\vec{R}\right)\frac{e^{ik_0R}}{4\pi R}, \quad \text{(A4)}$$

where $\vec{R} = \vec{r} - \vec{r}'$. $\vec{E}_{inc,\omega}$ is the sum of an external incident field and the field generated by the sources $\vec{J}^0_\omega(\vec{r}')$:

$$\vec{E}_{inc,\omega}(\vec{r}) = \vec{E}_{0,\omega}(\vec{r}) + i\omega\mu_0\int_V \bar{\bar{G}}_\omega(\vec{r},\vec{r}')\cdot\vec{J}^0_\omega(\vec{r}')d\vec{r}'. \quad \text{(A5)}$$

The resulting integral equation [Eq. (A3)] can be solved by discretization of the volume of the scatterers in N_s cells, according to the procedure detailed in Ref. [34]. The integral is transformed into a sum of N_s contributions corresponding to the cells used to discretize the objects. With algebraic manipulations, the electric field in the ith cell can be calculated by solving the following system of equations:

$$\overrightarrow{E}_i - \sum_{j=1,j\neq i}^{N_s}\overline{\overline{G}}_{i,j}\cdot\left[k_0^2\chi_j\overrightarrow{E}_j\right]\Delta\tau_j - k_0^2\chi_i\left(\overline{\overline{M}}_i - \frac{1}{k_0^2}\bar{\bar{L}}\right)\overrightarrow{E}_i$$
$$= \overrightarrow{E}_{inc,i}; \quad i,j = 1,2,\ldots,N_s, \quad \text{(A6)}$$

with

$$\overrightarrow{E}_{inc,i} = \overrightarrow{E}_{0,i} + i2\omega\mu_0 \times\left[\sum_{j=1,j\neq i}^{N_s}\overline{\overline{G}}_{i,j}\cdot\vec{J}^0_j\Delta\tau_j + \left(\overline{\overline{M}}_i - \frac{1}{k_0^2}\bar{\bar{L}}\right)\vec{J}^0_i\right], \quad \text{(A7)}$$

where $\bar{\bar{M}}$ and $\bar{\bar{L}}$ are correction 3×3 matrices meant to numerically handle the singularity added by the dyadic Green's function $\bar{\bar{G}}_{i,i}$ when the emitting and observing points coincide. More details on their derivation and evaluation are discussed in Ref. [34]. Here we report the values for a spherical mesh:

$$\overline{\overline{L}} = \frac{1}{3}\bar{\bar{I}},$$
$$\overline{\overline{M}}_i = \frac{2}{3k_0^2}\left[\left(1-ik_0R_i^{\text{eff}}\right)e^{ik_0R_i^{\text{eff}}} - 1\right]\overline{\overline{I}}, \quad \text{(A8)}$$
$$R_i^{\text{eff}} = \left(\frac{3}{4\pi}\Delta\tau_i\right)^{\frac{1}{3}},$$

where $\Delta\tau_i$ is the volume of the ith cell. Equation (A6) can be written in a compact form by taking advantage of matrix formalism

$$\bar{\bar{K}}\cdot\bar{X} = \bar{B}, \quad \text{(A9)}$$

where

$$\bar{X} = \left(E^x_1, E^x_2, \ldots, E^x_{N_s}, E^y_1, E^y_2, \ldots, E^y_{N_s}, E^z_1, E^z_2, \ldots, E^z_{N_s}\right), \quad \text{(A10)}$$

$$\bar{B} = \left(E^x_{inc,1}, E^x_{inc,2}, \ldots, E^x_{inc,N_s}, E^y_{inc,1}, E^y_{inc,2}, \ldots, E^y_{inc,N_s}, E^z_{inc,1}, E^z_{inc,2}, \ldots, E^z_{inc,N_s}\right), \quad \text{(A11)}$$

and $\bar{\bar{K}}$ is a $3N_s$ x $3N_s$ matrix operator defined in order to evaluate the left hand term in Eq. (A6) when it is applied to $\bar{X}$. The electric field inside the scatterers can be retrieved by the numerical solution of Eq. (A9):

$$\bar{X} = \bar{\bar{K}}^{-1}\cdot\bar{B}. \quad \text{(A12)}$$

Once the field inside the scatterers is evaluated, it is straightforward to calculate the electric field in any point of the spaces by solving the equation

$$\overrightarrow{E}_j = \overrightarrow{E}_{inc,j} + \sum_{i=1,j=N_s+1}^{N_s,N_t}\overline{\overline{G}}_{i,j}\cdot\left[k_0^2\chi_i\overrightarrow{E}_i\right]\Delta\tau_i;$$
$$\text{with } i = 1,2,\ldots,N_s; \text{ and } j = N_s+1, N_s+2,\ldots,N_t, \quad \text{(A13)}$$

where the points $i = 1,2,\ldots,N_s$ correspond to the cells used to discretize the scatterers and $\vec{E}_i$ is the electric field inside the scatterers, evaluated by solving Eq. (A12). Also, $j = N_s+1, N_s+2,\ldots,N_t$ is the index representing the points of space outside the scatterers, where we want to collect and evaluate the electric field. Since our aim is to calculate the mean thermal radiated power, the quantities of interest are not the mean radiated fields, but they are the flux and the energy density. We assume a stationary process, i.e., we consider a system in local thermal equilibrium. For the purpose of calculating ensemble-averaged mean radiated power in the far field, we need to calculate the cross spectral density, defined in Eq. (1). Indeed, in the far-field regime, the diagonal elements of the cross spectral density $\bar{\bar{W}}_\omega(\vec{r}_1,\vec{r}_1)$ are proportional to the mean radiated intensity density. According to Eq. (A10), numerical evaluation of $\bar{\bar{W}}_\omega(\vec{r}_1,\vec{r}_2)$ in the discretized mesh leads to the construction of the matrix $\langle\bar{X}\bar{X}^\dagger\rangle$. Using Eq. (A12) and performing algebraic manipulations, we obtain the result expressed in Eq. (2):

$$\langle\bar{X}\bar{X}^\dagger\rangle = \langle\bar{\bar{K}}^{-1}\bar{B}(\bar{\bar{K}}^{-1}\bar{B})^\dagger\rangle$$
$$= \bar{\bar{K}}^{-1}\langle\bar{B}\bar{B}^\dagger\rangle\bar{\bar{K}}^{-1^\dagger}. \quad \text{(A14)}$$

The matrix operator $\langle\bar{B}\bar{B}^\dagger\rangle$ contains the spectral correlation function of the current densities, which for a system in local thermal equilibrium is given by the fluctuation–dissipation theorem. It can be evaluated by observing that $\bar{B}$, defined in Eq. (A11), is an array containing the values of $\vec{E}_{inc,\omega}$ [see Eq. (A5)], calculated in the discretized mesh. The matrix operator $\langle\bar{B}\bar{B}^\dagger\rangle$ can be retrieved by the evaluation of $\langle\vec{E}_{inc,\omega}(\vec{r}_1)\vec{E}^\dagger_{inc,\omega'}(\vec{r}_2)\rangle$ on the mesh points. Since no other external deterministic field is considered, we have

$$\langle\vec{E}_{inc,\omega}(\vec{r}_1)\vec{E}^\dagger_{inc,\omega'}(\vec{r}_2)\rangle$$
$$= \mu_o^2\,\omega^2\int\overline{\overline{G}}_\omega(\vec{r}_1,\vec{r}')\,\overline{\overline{G}}^\dagger_{\omega'}(\vec{r}_2,\vec{r}'')\left\langle\vec{J}^0_\omega(\vec{r}')\,\vec{J}^{0\dagger}_{\omega'}(\vec{r}'')\right\rangle d\vec{r}'d\vec{r}'', \quad \text{(A15)}$$

where $\langle\vec{J}^0_\omega(\vec{r}')\,\vec{J}^{0\dagger}_{\omega'}(\vec{r}'')\rangle$ is defined in Eq. (5).

Once the operators $\bar{\bar{K}}$ and $\langle \bar{B}\bar{B}^{\dagger} \rangle$ have been evaluated, $\langle \bar{X}\bar{X}^{\dagger} \rangle$ can be calculated by performing products of matrices, as shown in Eq. (2), and its diagonal elements can be used to calculate Eq. (7). Calculation of Eq. (A15) requires a careful analysis, similar to the one performed for standard scattering [35], because of the divergence of the Green dyadic for $\vec{r}' = \vec{r}_1$, $\vec{r}'' = \vec{r}_2$ and $\vec{r}' = \vec{r}_1 = \vec{r}'' = \vec{r}_2$. The main difference between our method and the one described in Ref. [26] is based on the fact that we do not assume $E_{\text{inc}} = 0$ inside the emitters. Indeed this assumption cannot be made if the size of the object is smaller or comparable to the penetration depth of the EM wave in the considered material. This is the core of our discussion because all the peculiar properties in the emission pattern and the enhancement with respect to macroscopic structures are related to the excitation of localized surface plasmon polaritons and coupling between evanescent waves. Finally, the numerical method could be extended in order to consider NA arrays embedded in layered media, such as planar waveguides, by combining the VIE method with the numerical evaluation of the Green dyadic for layered media [35].

[1] Z. M. Zhang, *Nano/Microscale Heat Transfer* (McGraw-Hill, New York, 2007).

[2] S. Volz (ed.), *Thermal Nanosystems and Nanomaterials*, Topics in Applied Physics Vol. 118 (Springer-Verlag, Berlin, 2009).

[3] K. Joulain, J. P. Mulet, F. Marquier, R. Carminati, and J. J. Greffet, Surface electromagnetic waves thermally excited: Radiative heat transfer, coherence properties and Casimir forces revisited in the near field, Surf. Sci. Rep. **57**, 59 (2005).

[4] X. Liu, L. Wang, and Z. M. Zhang, Near-field thermal radiation: Recent progress and outlook, Nanoscale and Microscale Thermophysical Engineering, **19**, 98 (2015).

[5] A. Ishikawa and T. Tanaka, Metamaterial absorbers for infrared detection of molecular self-assembled monolayers, Sci. Rep. **5**, 12570 (2015).

[6] X. Liu, T. Tyler, T. Starr, A. F. Starr, N. M. Jokerst, and W. J. Padilla, Taming the Blackbody with Infrared Metamaterials as Selective Thermal Emitters, Phys. Rev. Lett. **107**, 045901 (2011).

[7] A. P. Raman, M. A. Anoma, L. Zhu, E. Rephaeli, and S. Fan, Passive radiative cooling below ambient air temperature under direct sunlight, Nature **515**, 540 (2014).

[8] J. K. Tong, W.-C. Hsu, Y. Huang, S. V. Boriskina, and G. Chen, Thin-film 'thermal well' emitters and absorbers for high-efficiency thermophotovoltaics, Sci. Rep. **5**, 10661 (2015).

[9] A. Lenert, D. M. Bierman, Y. Nam, W. R. Chan, I. Celanović, M. Soljačić, and E. N. Wang, A nanophotonic solar thermophotovoltaic device, Nature Nanotechnology **9**, 126 (2014).

[10] I. E. Khodasevych, L. Wang, A. Mitchell, and G. Rosengarten, Micro- and nano-structured surfaces for selective solar absorption, Adv. Opt. Mat. **3**, 852 (2015).

[11] J. B. Pendry, Radiative exchange of heat between nanostructures, J. Phys.: Condens. Matter **11**, 6621 (1999).

[12] P. Ben-Abdallah and S.-A. Biehs, Many-Body Radiative Heat Transfer Theory, Phys. Rev. Lett. **107**, 114301 (2011).

[13] D. Polder and M. Van Hove, Theory of radiative heat transfer between closely spaced bodies, Phys. Rev. B **4**, 3303 (1971).

[14] J. R. Howell, M. P. Menguc, and R. Siegel, *Thermal Radiation Heat Transfer*, 5th ed. (CRC Press, Boca Raton, Florida, 2011).

[15] S. M. Rytov, Y. A. Kravtsov, and V. I. Tatarskii, *Principles of Statistical Radio-Physics 3* (Springer-Verlag, Berlin, 1989).

[16] S. Shen, A. Narayanaswamy, and G. Chen, Surface phonon polaritons mediated energy transfer between nanoscale gaps, Nano Lett. **9**, 2909 (2009).

[17] S.-A. Biehs, M. Tschikin, R. Messina, and P. Ben-Abdallah, Super-Planckian near-field thermal emission with phonon-polaritonic hyperbolic metamaterials, Appl. Phys. Lett. **102**, 131106 (2013)

[18] A. Reiser and L. Schachter, Geometric effects on blackbody radiation, Phys. Rev. A **87**, 033801 (2013).

[19] C. Wuttke and A. Rauschenbeutel, Thermalization via Heat Radiation of an Individual Object Thinner than the Thermal Wavelength, Phys. Rev. Lett. **111**, 024301 (2013).

[20] C. Wu, N. Arju, G. Kelp, J. A. Fan, J. Dominguez, E. Gonzales, E. Tutuc, I. Brener, and G. Shvets, Spectrally selective chiral silicon metasurfaces based on infrared Fano resonances, Nat. Comm. **5**, 3892 (2014).

[21] J. A. Schuller, T. Taubner, and M. L. Brongersma, Optical antenna thermal emitters, Nat. Phot **3**, 658 (2009).

[22] S. Ingvarsson, L. J. Klein, Y. Y. Au, J. A. Lacey, and H. F. Hamann, Enhanced thermal emission from individual antenna-like nanoheaters, Opt. Express **15**, 11249 (2007).

[23] M. Husnik, S. Linden, R. Diehl, J. Niegemann, K. Busch, and M. Wegener, Quantitative Experimental Determination of Scattering and Absorption Cross-Section Spectra of Individual Optical Metallic Nanoantennas, Phys. Rev. Lett. **109**, 233902 (2012).

[24] G. Biener, N. Dahan, A. Niv, V. Kleiner, and E. Hasman, Highly coherent thermal emission obtained by plasmonic bandgap structures, Appl. Phys. Lett. **92**, 081913 (2008).

[25] B. J. Lee, C. J. Fu, and Z. M. Zhang, Coherent thermal emission from one-dimensional photonic crystals, Appl. Phys. Lett. **87**, 071904 (2005).

[26] S. Edalatpour and M. Francoeur, The thermal discrete dipole approximation (T-DDA) for near-field radiative heat transfer simulations in three-dimensional arbitrary geometries, J. Quant. Spectrosc. Radiat. Transfer **133**, 364 (2014).

[27] A. W. Rodriguez, O. Ilic, P. Bermel, I. Celanovic, J. D. Joannopoulos, M. Soljačić, and S. G. Johnson, Frequency-Selective Near-Field Radiative Heat Transfer Between Photonic Crystal Slabs: A Computational Approach for Arbitrary Geometries and Materials, Phys. Rev. Lett. **107**, 114302 (2011).

[28] A. G. Curto, T. H. Taminiau, G. Volpe, M. P. Kreuzer, R. Quidant, and N. F. van Hulst, Multipolar radiation of quantum emitters with nanowire optical antenna, Nature Comm. **4**, 1750 (2013).

[29] S. M. Hein and Harald Giessen, Tailoring Magnetic Dipole Emission with Plasmonic Split-Ring Resonators, Phys. Rev. Lett. **111**, 026803 (2013).

[30] E. D. Palik, *Handbook of Optical Constants of Solids* (Academic Press, Inc., Orlando, Florida, 1985).

[31] C. F. Bohren and D. R. Huffman, *Absorption and Scattering of Light by Small Particles* (Wiley, New York, 1983).

[32] G. W. Bryant, F. J. Garcìa de Abajo, and J. Aizpurua, Mapping the plasmon resonances of metallic nanoantennas, Nano Lett. **8**, 631 (2008).

[33] B. Rolly, B. Stout, and N. Bonod, Boosting the directivity of optical antennas with magnetic and electric dipolar resonant particles, Opt. Express **20**, 20376 (2012).

[34] O. J. F. Martin and N. B. Piller, Electromagnetic scattering in polarizable backgrounds, Phys. Rev. E **58**, 3909 (1998).

[35] M. Paulus, P. Gay-Balmaz, and O. J. F. Martin, Accurate and efficient computation of the Green's tensor for stratified media, Phys. Rev. E **62**, 5797 (2000).